Journal of Materials Chemistry A

ROYAL SOCIETY OF CHEMISTRY

PAPER

View Article Online
View Journal | View Issue

Cite this: J. Mater. Chem. A, 2024, 12, 15847

Combining NMR and impedance spectroscopy *in situ* to study the dynamics of solid ion conductors†

Sheyi Clement Adediwura, Neeshma Mathew and Jörn Schmedt auf der Günne *

Received 13th October 2023
Accepted 23rd May 2024

DOI: 10.1039/d3ta06237f

rsc.li/materials-a

Differences in activation energies of solid ion conductors as measured by different techniques can be either considered a consequence of experimental uncertainty or a valuable source of information about the local ion transport mechanism. Here, it is suggested that an *in situ* combination of solid-state nuclear magnetic resonance (NMR) and electrochemical impedance spectroscopy (EIS) helps to differentiate these two cases because the sample preparation and thermal history are then identical for the NMR and EIS measurement. To this end, an *in situ* NMR–EIS probe head is developed, calibrated and its performance is tested on the lithium-ion conductor Li_8SnO_6. For validation, the results were compared to carefully conducted *ex situ* measurements. The differences in activation energies as observed by NMR and EIS experiments could in this case be confirmed and rationalized by comparison to results from nudged elastic band calculation using density functional theory under periodic boundary conditions.

1 Introduction

The progress of solid-state batteries is strongly correlated to the discovery of solid ion conductors with high ionic conductivity of $>10^{-2}$ S cm^{-1} at room temperature.[1–3] Improving the ion transport efficiency and capacity retention in solid-state batteries requires a holistic understanding of the conduction mechanism, especially concerning ion transport across the electrolyte/electrode interface.[2–4] Several techniques have been deployed to characterize the ion transport properties of solid materials at different length and time scales.[5–7] The commonly used approaches to determine the ionic conductivity and diffusion properties of materials are: electrochemical impedance spectroscopy (EIS) which probes long-range charge transport in the bulk and at interfaces,[8] NMR diffusometry which probes long-range diffusion,[9,10] line-shape and spin-alignment echo solid-state nuclear magnetic resonance spectroscopy probe ionic motion on a short to medium range,[11–13] and the conventional spin–lattice relaxometry solid-state nuclear magnetic resonance spectroscopy which probes short-range motion.[11,14]

Together, these techniques provide a comprehensive understanding of the charge and mass transport associated with ionic motion. The respective activation energies for mass and charge transport, which are obtained from experiments conducted at different temperatures, provide an insight into whether the corresponding motional processes leading to mass and charge transport are identical. A literature review reveals in several cases differences in activation energies from impedance and nuclear magnetic resonance spectroscopy.[13,15–17] While there is often a good agreement within error limits, differences remain a valuable source of information especially when techniques with different inherent time and length scales explore the complicated energy landscape featuring one or more barriers of disordered ionic conductors.[18] While some of the differences can be explained by the different length and time scales of the techniques, even between different NMR techniques used to study macros- and microscopic transport,[5,13] differences in activation energy can also just be a consequence of the experimental conditions (see below). According to a recent round-robin test[19] conducted on six reference compounds in the form of a powder, the measured ionic conductivity for the same material varies by about one order of magnitude between eight participating laboratories around the world. It is not unreasonable to assume that also activation energies are subject to sizeable errors, especially because variable temperature and pressure conditions used in impedance spectroscopy can lead to processes modifying the grain boundaries.[20–22] Furthermore, some of these changes are not detectable by certain routine structural characterisation techniques such as X-ray diffraction for after-effect analysis.[20]

Department of Chemistry and Biology, Faculty IV: School of Science and Technology, Inorganic Materials Chemistry and Center of Micro- and Nanochemistry and Engineering (Cμ), University of Siegen, Adolf-Reichwein-Straße 2, 57068 Siegen, Germany. E-mail: gunnej@chemie.uni-siegen.de

† Electronic supplementary information (ESI) available: Information about 3D printing, synthesis, powder X-ray diffraction, technical details about alternating current filters, electronic details of the *in situ* cell, probe head, detailed fitting results of impedance spectra and details about nudged elastic band calculations. See DOI: https://doi.org/10.1039/d3ta06237f

Discrepancies between activation energies from different methods are in fact common place. As an example for the fast Li-ion conductor $Li_7La_3Zr_2O_{12}$, the reported values are 0.3–0.34 eV measured by impedance spectroscopy,[23] 0.53 eV by spin-alignment echo NMR,[24] 0.43 eV by line shape NMR and 0.32–0.48 eV by spin–lattice relaxometry NMR,[25] while 0.33–0.36 eV and 0.26 eV were predicted by initio molecular dynamics simulation,[26,27] and by nudged elastic band calculations,[28] respectively. Another less prominent example is the Li-rich phase Li_8SnO_6,[29,30] which will serve as a test case for this contribution, for which a consistent interpretation of the different reported activation energies (NMR: 0.31 eV,[31] EIS: 0.91 eV,[31] quantum chemistry: 0.43–1.40 eV,[32] forcefield calculations: 0.20–1.06 eV (ref. 33)) is still missing. The structure of Li_8SnO_6 is surprisingly complicated in the sense that it features two different Li sites with an octahedral and a tetrahedral coordination polyhedron which are a potential source of dynamic heterogeneity of the Li motion.[30,32,33]

One way to overcome the experimental uncertainties related to the determination of activation energies is to change from *ex situ* to *in situ* NMR–EIS measurements so that differences cannot be blamed on sample related changes. To the best of our knowledge, such a setup has not been reported yet, which may be related to the problems associated with separating the required electromagnetic waves whose frequencies are only different by one order of magnitude. Technically much simpler is the separation of a direct current channel from an NMR frequency channel, which in the context with batteries is known as operando NMR. It provides insight into electrode materials while charging and discharging, so that metastable intermediates and structural changes could be identified:[34–42] For the anode it could be shown that the structure of graphite intercalation compounds correlated with the charge state.[35–39] Lithium dendrites, which need to be avoided can be traced in the early stages.[42] Silicon as anode material or as an additive to carbon-based anodes could be studied[40] to identify intermediates at different states of charging. In this context, the combination with *ex situ* EIS was important[41] to get a better understanding of the cell resistance as a function of the charging state of the battery.

The target of this contribution is to develop an *in situ* NMR–EIS setup, evaluate its performance by comparing *ex situ* and *in situ* measurements and demonstrate its advantages on the example of the compound Li_8SnO_6.

2 Experimental part

2.1 3D printing

All models were designed using FreeCAD v0.20 software, then sliced with Ultimaker cura v5.1.0 and Intamsuite v3.7.0. The prototypes were developed using a Creality CR-10s 3D printer, (Cordol Technology Co., Limited) and the final version was printed with a high-temperature 3D printer, INTAMSYS FUNMAT HT (INTAMSYS). The printers were configured as shown in (Table S1†). All prototypes were printed with a hardened steel nozzle with 0.4 mm diameter at 0.1 mm layer height which is a compromise between printing quality and time. The high temperature version was printed with a nozzle with a 0.25 mm diameter using the same layer height as the prototypes. Parts with thermoplastic filaments were sintered in an oven at a temperature of 473 K for 2 hours to increase their thermal strength. The printed parts were afterwards incorporated into a home-built static probe head based on a McKay design.

2.2 Sample preparation and characterization

2.2.1 Solid state synthesis. Li_8SnO_6 was synthesized *via* a solid-state synthesis route using Li_2O (Alfa Aesar, 99.95%) and SnO_2 (Carl Roth, ≥99.5%) as starting materials. Li_2O was stored inside the glove box (MBraun) under an argon atmosphere. Li_2O (1002.0 mg, 33.53 mmol) and SnO_2 (900.0 mg, 5.97 mmol) were thoroughly mixed and ground using a mortar and pestle immediately after taking Li_2O out of the glove box. The ground mixture was pressed into a pill and then heated to 1173 K at a heating rate of 20 K min^{-1}, then annealed at 1173 K for 20 hours and then cooled down to room temperature at a cooling rate of 10 K min^{-1}. An excess of 40 wt% Li_2O was used to compensate for the lithium loss during the synthesis. The synthesis of $Li_{1.5}Al_{0.5}Ge_{1.5}(PO_4)_3$ is described in the ESI.†

2.2.2 Powder X-ray diffraction. Powder X-ray diffraction was carried out with a Guinier camera (Huber G621) with Cu Kα_1 radiation (λ = 1.54056 Å). A silicon dioxide standard (Quarzwerke Dörentrup "alpha SiO_2 quartz", a finely ground standard for XRD, a = 4.9136 Å, c = 5.4054 Å) was used as a reference sample. IPreader software[43] was used for data extraction and TOPAS academic software package v.4 (ref. 44) for Rietveld refinement and quantitative phase analysis of the sample.

2.2.3 *Ex situ* NMR spectroscopy. The chemical shift values of ^{7}Li are reported on a deshielding scale, relative to the resonance of a solution of LiCl in D_2O (9.7 mol kg^{-1}). The ^{1}H NMR resonance of 1% (mass) $Si(CH_3)_4$ in $CDCl_3$ served as an external secondary reference using the Ξ values ^{7}Li as reported by the IUPAC[45,46] for solid-state NMR measurements. The ^{7}Li NMR spin alignment echo and single pulse experiments of a static powder were measured on a Bruker Avance II spectrometer at a magnet field of 7.0 T at a resonance frequency of 116.64 MHz. The sample was kept in an evacuated quartz ampoule with an outer diameter of 3 mm and a length of 25 mm. ^{7}Li spin alignment echo experiments were recorded using a Jeener–Broekaert pulse sequence ($90° - t_p - 45° - t_m - 45°$)[47] at an evolution time t_p of 15 μs as a function of the mixing time $0 \leq t_m \leq 512$ ms, using an 8-step phase cycle.[48] The recycle delay was set to $5T_1$ and the dead time delay $\tau_{deadtime}$ was 15 μs. The decay curves were fitted using a stretched exponential function,[49]

$$S(t_m) = (1 - S_0)\exp\left(-\left(\frac{t_m}{\tau}\right)^{\beta}\right) + S_0$$

to estimate the lithium ion jump rate $1/\tau$, where S_0 is the final state correlation value and β is the stretching factor. The spin alignment echo measurements were conducted at sufficiently high temperatures to separate the contributions of quadrupolar spin–lattice relaxation T_{1Q} from contributions from individual jumps of the spins between electrically non-equivalent

crystallographic orbits. The NMR signals were deconvoluted and their second moments of the lineshape were determined using Deconv2DXY v0.7,[50] while the lithium ion jump rates $1/\tau$ from spin alignment echo decay curves were analysed using home written python script based on SciPy libraries.[51]

2.2.4 *Ex situ* electrochemical impedance spectroscopy. The Li_8SnO_6 powder sample was thoroughly ground in an agate mortar and pressed into a cylindrical pellet (diameter = 8 mm) applying a pressure of 585 MPa for 20 min. It was heated to 873 K at a rate of 5 K min^{-1} and kept there for 3 hours. The thickness of the pellet was measured with an electronic micrometre screw gauge. The pellets were mounted inside a 3D-printed sputtering shield and gold was sputtered onto both sides using a sputter coater (108 Auto, Cressington). Electrochemical impedance spectroscopy (EIS) measurements were recorded using NEISYS electrochemical impedance analyser (Novocontrol Technologies) in a home-built cell, which was calibrated before actual measurements based on short/load calibration standards with 100 Ω resistor as the load. The impedance measurements were recorded in potentiostatic mode, with a perturbation signal of 35 mV_{rms} amplitude, in a frequency range from 30 mHz to 1 MHz. The temperature was controlled using a variable temperature and flow controller (NMR Service GmbH) with a constant nitrogen gas flow. Each temperature point was held for 10 min to ensure thermal equilibrium with an accuracy of ±0.1 K throughout the EIS measurement. The data analysis was performed using home-written python scripts based on the SciPy libraries.[51]

2.2.5 *In situ* NMR–EIS experiments. The conditions of the NMR and EIS experiments of the *in situ* experiments follow the procedures and conditions of the corresponding *ex situ* experiments if not mentioned in the following. To prevent the EIS circuit from acting as an antenna and introducing noise to the NMR resonator, low-pass filters were connected to the EIS channel. Each of the four cables of the EIS channel was passed through a separate low-pass filter. Because the impedance spectrometer cannot be positioned close to the NMR magnet, longer cables of about 5 m length connecting the sample cell to the impedance spectrometer were used. These modifications required a recalibration of the *in situ* EIS setup, which was performed using special short/load standards produced for this cell.

2.3 Quantum chemistry

The plane wave pseudopotential method based on density functional theory under periodic boundary conditions as implemented in Quantum Espresso (QE) 6.8 (ref. 52) was utilised to estimate activation energies of the lithium-ion diffusion pathways in Li_8SnO_6. The crystal structure of Li_8SnO_6 in the space group *R*3 (hexagonal axes, ICSD collection code 28 131)[29] served as a structure model. The cif file of Li_8SnO_6 was converted into an input file using cif2cell 2.0.0 (ref. 53) for the QE calculations. Vacancy models were generated using a compensating background charge and all fractional coordinates were allowed to relax. The QE calculations employed pseudopotentials of the GBRV type[54,55] and *k*-point selection followed the Monkhorst–Pack scheme.[56] The presented simulations used a 2 × 2 × 3 *k*-mesh and a supercell containing 180 atoms (convergence error 0.001 eV). The supercells were optimized to the most stable configuration by setting up a kinetic energy cut-off of 480 eV and 60 eV for the charge density cut-off (convergence error ~0.01 eV). Climbing Image-Nudged Elastic Band (CI-NEB) calculations using QE were performed to calculate the activation energy of a vacancy moving from one Li position to a neighbouring one.[57] Eight intermediate images were used along with the first and last images to identify the diffusion pathway for the Li-ion transport. These calculations provide an estimate for the saddle-point of the movement of the vacancy between Li sites, *i.e.* the minimum energy path in the energy-hypersurface and thus an estimate for the activation energy.

3 Results and discussion

An *in situ* NMR–EIS technique (Fig. 1) requires a setup in which nuclear magnetic resonance and impedance spectroscopy can be conducted at different temperatures on the same compound. To show such a setup is functional, in the first two parts of this chapter.

1. Design, fabrication and calibration of the *in situ* NMR–EIS probe head and

2. Validation: *ex situ versus in situ* measurements on Li_8SnO_6 will be presented. Finally, the experimental results for the activation energies will be compared to

3. Activation energies for Li_8SnO_6 from quantum chemical calculations.

3.1 *In situ* NMR–EIS probe head

The design targets for the *in situ* NMR–EIS probe head can be described as follows. The probe head needs to separate a high

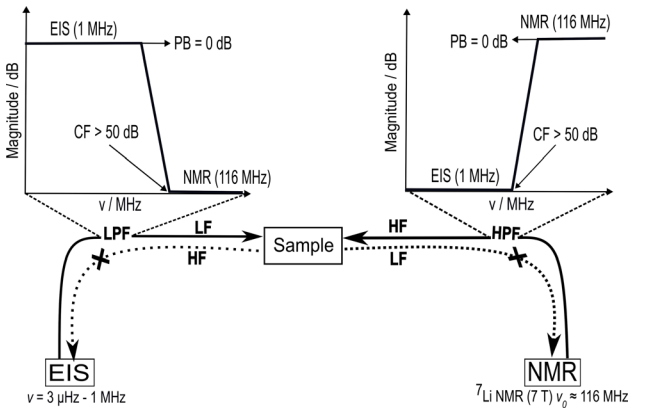

Fig. 1 Sketch of the *in situ* NMR–EIS setup to perform electrochemical impedance spectroscopy (EIS) and solid-state nuclear magnetic resonance (NMR) spectroscopy on the same sample. This technique requires a sufficient electrical separation of the high-frequency (HF) channel, operating at the NMR (Larmor) frequency ν_0 of 116 MHz in the presented work, and the low-frequency (LF) channel for EIS operating in a frequency range between 3 μHz and 1 MHz. This separation requires low-pass and high-pass filters on the opposite channels to achieve an attenuation of at least 50 dB at the cut-off frequency while the pass-band remains unattenuated (<0.05 dB) up to frequencies required for the *in situ* measurements.

(NMR) from a low (EIS) frequency channel, which is achieved by introducing electrical high and low pass filter elements into the circuits. The probe head needs to cope with an extended cable length of about 5 m on the EIS side which is a consequence of the required distance to the superconducting magnet. The sample cell must allow variable temperatures, provide a reproducible and stable contact for the EIS electrodes and have a sufficiently big frequency range to conduct impedance spectroscopy measurements. While the design targets may look similar to the ones of an *in situ* NMR battery cycler, the proximity of the frequency ranges of the two channels of the *in situ* EIS–NMR probe head requires other solutions, including a different design of the sample cell, calibration and filter specifications (see below).

By design (Fig. 2), the sample sits in between two metallic electrodes connected to an impedance spectrometer inside a solenoid coil. Considering the skin depth associated with a radio frequency pulse and the magnetic susceptibility difference of the materials,[58,59] this configuration is expected to have both an inhomogeneity in the pulse B_1 and magnetic field B_0.

Additionally, the sample cell design is problematic because a sensitive NMR resonator with a high filling factor would typically require a solenoid coil while impedance spectroscopy would imply the sample is inserted between two electrodes. An *in situ* NMR–EIS sample cell was developed with good mechanical properties for a temperature range from 160 K to 473 K (Fig. 3), which provides a good electrical contact for impedance measurements and a high filling factor for NMR. To ensure the *in situ* sample cell is air-tight and suitable for moisture-sensitive samples, high-temperature o-rings were incorporated into the sample cell. The development profited from rapid prototyping which was possible because the cell was produced using 3D printing of thermoplastic filaments (*i.e.* polyether ether ketone and polyphenylene sulfone). The latter was especially relevant to optimize gas and temperature flow within the probe head to achieve low temperature gradients over the sample and a quick response of the sample temperature on a temperature change of the flowing N_2 gas. To this end, the wall thickness of the sample cell was reduced to only 0.7

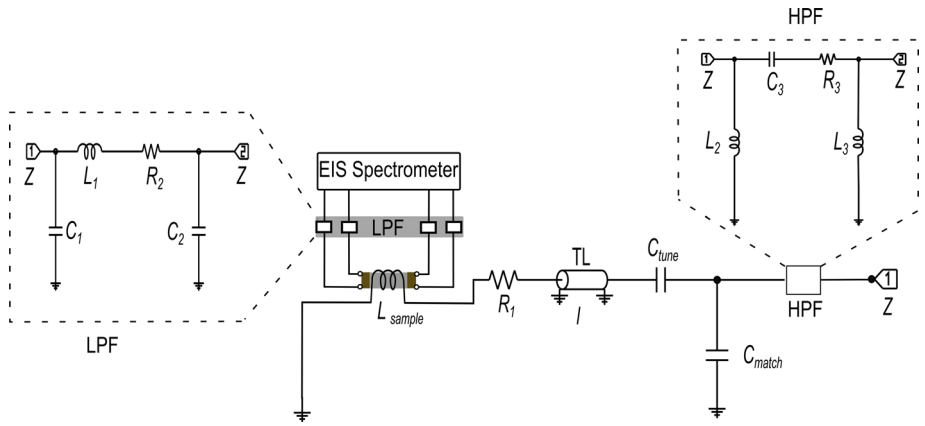

Fig. 2 Schematic circuit diagram of ^{7}Li single resonance *in situ* NMR–EIS probe with a solenoid coil for the NMR wide-bore magnet. The NMR circuit was tuned and matched with the help of the variable capacitors C_{tune} and C_{match} to the resonance frequency of ^{7}Li of 116.64 MHz. Inductor L_{sample} represents the sample coil, the resistor R_1 represents losses in the coil and remaining circuit, and l is the length of a transmission line (TL). The low-pass and high-pass filter circuits (LPF and HPF) are shown with dotted outline, connected to the EIS and NMR channels, respectively. The circuits' components consist of capacitors C_1–C_3, resistors R_2–R_3, and inductors L_1–L_3. Details about simulation and fabrication of the filters are in the ESI (Section S2, and Fig. S1(a–f)).† The impedance Z of the *in situ* NMR–EIS probe circuit was matched to 50 Ω.

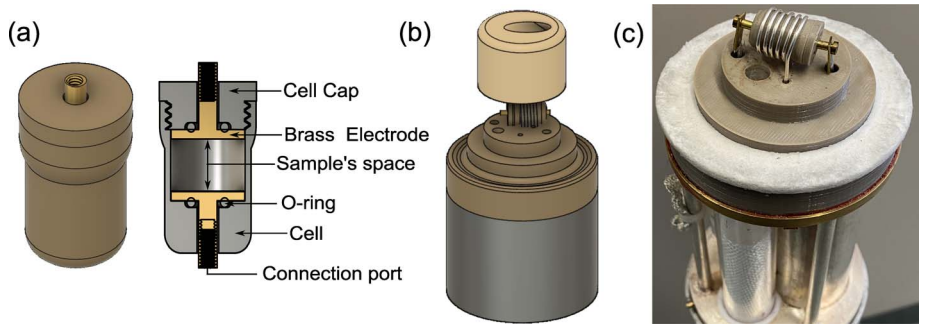

Fig. 3 Photos and diagrams for the *in situ* NMR–EIS probe head. (a) 3D model of the *in situ* sample cell, printed with polyether ether ketone filament. (b) 3D model of the *in situ* probe head top part, showing the location of the sample cell in the solenoid coil for the detection of the NMR signal and the top insulation cap for variable-temperature experiments, printed with polyphenylene sulfone filament. (c) Photograph of the mounted sample cell already connected to the EIS channel.

mm. The 3D-printed top parts for the variable-temperature experiment allow temperatures up to 473 K.

The presented *in situ* NMR–EIS probe head employs McKay design: a remote tunable single coil transmission line NMR probe head, similar to other probe heads used in the group including a symmetrizing capacitor (Fig. 3c).[60] The *in situ* NMR–EIS probe head was used only in single channel mode. Because in the *in situ* probe head, both channels are connected to the same sample, a good separation of the high-frequency (NMR: 116.6 MHz) and of the low-frequency (EIS: 1 MHz–30 mHz) channel is compulsory: Both channels will mutually add noise and artefacts to the other channel which is not wanted. A simple solution is to add passive LCR filters which block the unwanted channel with at least 50 dB attenuation and have a flat passband (<0.05 dB). In fact losses in the EIS channel are less critical than ripple in the passband. The filters were realized as passive 3-element filters and are described in detail in the ESI (low pass-filter Fig. S1(a), high-pass filter Fig. S1(d)).† Each of the four cables connecting the impedance spectrometer and the measurement cell was equipped with a shielded separate filter box connected *via* BNC connectors. These cables needed to be longer (length 5 m) than in the *ex situ* setup to position the EIS spectrometer in at sufficient distance from the magnet.

The modifications required for the *in situ* setup make calibration of the impedance spectrometer compulsory. This was achieved using a short/load calibration[61] against standards fabricated for the developed measurement cell (Fig. S3†). The validation results of the calibration procedures (Section S3†) confirm that the residual fixtures of the extended measurement cables and low pass filters were effectively isolated from the sample's impedance measurement and that the *in situ* NMR–EIS probe head was successfully calibrated. We did not succeed in calibrating the cell with 2-element passive filters but only with the aforementioned 3-element filters (Fig. S1†). The calibration was further tested using the compound $Li_{1.5}Al_{0.5}Ge_{1.5}(PO_4)_3$, for which impedance spectra were obtained with an *ex* and *in situ* cell which only differed by 0.3% (estimate from five separate measurements, Fig. S4, and Table S2†).

Finally, the performance of the new *in situ* NMR–EIS probe head (Fig. S5†) was experimentally tested on standard parameters including impedance measurement stability, nutation frequency, *in situ* NMR–EIS measurement stability, interference suppression, operating temperature range (160–473 K) and extended time thermal stability with good results. A nutation frequency of 19 kHz was estimated from a ^{7}Li NMR nutation curve measurement for LiCl (Fig. S6†). The nutation curve shows a rather fast decay which is due to a pulse field inhomogeneity as expected from the use of a metallic electrode necessary for the EIS measurement. Thermal equilibrium could be achieved within 5 min for variable temperature measurements.

3.2 *Ex situ versus in situ* EIS–NMR experiments on Li_8SnO_6

The test compound Li_8SnO_6 was synthesised *via* a solid state synthesis route to demonstrate the *in situ* EIS–NMR technique and to validate the setup. The crystalline phase was identified by X-ray diffraction (Fig. S7†). The compound purity is determined to be higher than 99% with a side phase of Li_2O, according to a Rietveld refinement of X-ray diffraction data. *Ex situ* ^{7}Li single pulse NMR spectra of Li_8SnO_6 were recorded in a static mode at different temperatures (Fig. 4), to monitor the effect of lithium ion jumps on the ^{7}Li spectral lineshape. At low temperatures below 300 K, the central transition peak is broadened by dipolar interactions. The central transition of the spectrum in the first approximation is independent of the quadrupolar interaction and determined by the dipolar interaction.[11] As the temperature increases, the ^{7}Li NMR line shape of the central transition starts to narrow as a consequence of translational ionic motion. This motional narrowing effect in the central transition occurs when the jump rate of the mobile species is of the order of the square root of the dipolar second moment.[11] Along with the broad central transition, satellite transitions from the two different Li sites are also visible which in principle could allow study of lithium ion motion on octa- and tetrahedral Li sites independently. Because of the limited resolution and only small changes, we have not further investigated temperature induced changes in the satellite transitions.

The line-width of the central transitions of the ^{7}Li atoms was estimated from the second moment of the central transition peak as a function of temperature (Fig. 4b). For Li_8SnO_6 a flat low-temperature plateau is observed, which justifies the simplified treatment according to Waugh and Fedin,[62,63] who found that the onset temperature T_{onset} of line-narrowing is linearly related to the activation energy $E_A = 1.617$ meV $K^{-1} \cdot T_{onset}$ with an estimated error of 10%. The *in situ* NMR line shape analysis is similar to the *ex situ* measurements (Fig. 4). The obtained activation energies from *ex situ* and *in situ* lineshape analysis of Li_8SnO_6 agree within error limits (Table 1).

An independent source of information to study Li-motion are spin-alignment experiments.[48,49,64] The ^{7}Li spin alignment echo NMR amplitudes $S(T,t_m)$ of Li_8SnO_6 were recorded for both *ex situ* and *in situ* at different mixing times t_m and temperatures T. The decay curves are not affected by the quadrupolar spin–lattice relaxation T_{1Q}, but rather solely by lithium ion jumps between different crystallographic orbits in the Li_8SnO_6.[49,65] The quadrupolar spin–lattice relaxation induces two-step decay curves at low temperatures; thus, spin alignment echo measurements were performed at higher temperatures (Fig. 5a and c). The lithium ion jump rates $1/\tau$ determined from *ex situ* and *in situ* measurements follow an Arrhenius law $\tau^{-1} = \tau_0^{-1} \exp(-E_A/(k_B T))$.[49,65] Here, E_A is the estimated activation energy, τ_0 is the pre-exponential factor and k_B is the Boltzmann constant.

The *ex situ* activation energy is 0.61(1) eV while the *in situ* activation energy is also 0.58(1) eV. The calculated jump rates τ^{-1} vary from 196 s^{-1} to 16 667 s^{-1} at temperatures from 363 to 463 K, respectively. The pre-exponential factor is consistent with low diffusion coefficients and the results from impedance spectroscopy (*vide infra*). An excellent agreement between the results from the *in situ* and the *ex situ* setup is observed (Fig. 5).

Macroscopic lithium ion conductivities were investigated by impedance spectroscopy using two ion blocking gold electrodes. The complex impedance spectra (example Fig. 6) exhibit typical characteristics (with up to two half-circles at sufficiently

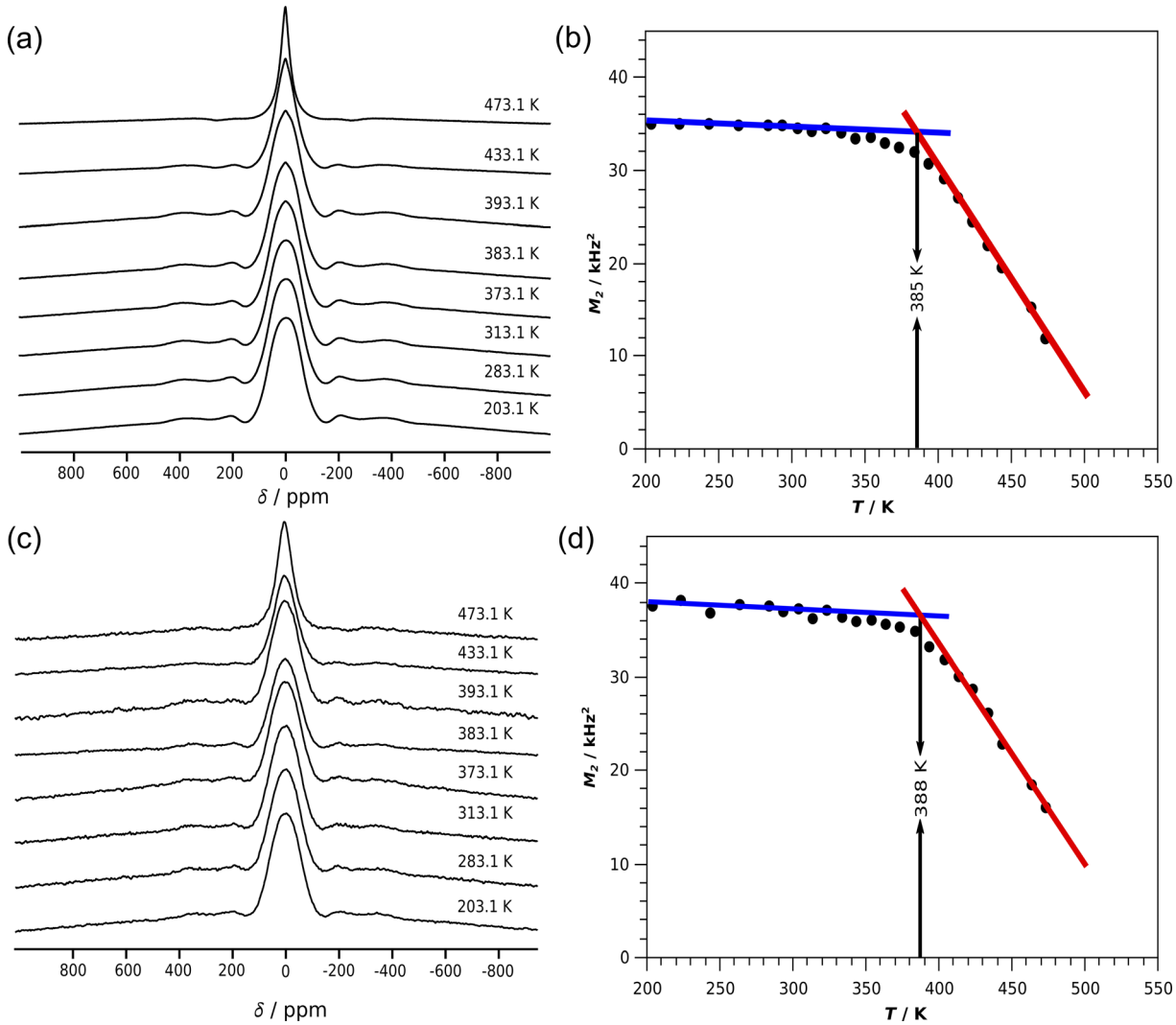

Fig. 4 ^{7}Li NMR spectra of Li_8SnO_6 of static powder samples measured at a frequency of 116.643 MHz (a) using *ex situ* NMR probe head (c) using the developed *in situ* NMR–EIS probe head at different (selected) temperatures. The second moment M_2 calculated from the central transition of a baseline corrected spectrum for temperatures ranging from 203.1 to 473.1 K (b) using an standard NMR probe head for *ex situ* measurements and (d) using the developed *in situ* NMR–EIS probe head. The onset temperatures were estimated from the crossover of the red and blue lines.

Table 1 Onset temperatures T_{onset} obtained from lineshape analysis of the ^{7}Li NMR spectra (Fig. 4) of Li_8SnO_6 and activation energies E_A calculated using the Waugh and Fedin[62,63] equation for *in situ* and *ex situ* techniques

NMR line shape analysis technique	T_{onset}/K	E_A/eV
Ex situ	385	0.62(6)
In situ	388	0.63(6)

low temperature) of an electrically inhomogeneous solid ion conductor, where the grain boundary resistance dominates the overall impedance.[8] The impedance spectra were modelled with an equivalent circuit (Fig. 6 inset) consisting of a series connection of two parallel arrangements of a resistor R and a constant phase element Q, depicting the conductive and capacitive characteristics of the bulk and grain boundary regions of the solid ion conductor, respectively.[8] The electrode polarisation is modelled using additional constant phase element Q.[8] The effective capacitance C_{eff} of the constant-phase element is calculated using Brug's formula $C_{eff} = (Q \cdot R^{(\alpha-1)})^{(1/\alpha)}$.[66] From the equivalent circuit analysis of the impedance data, the high frequency arc (Fig. 6) corresponds to a capacitance of 7.61 pF, thus depicting the bulk region of the sample while the mid-frequency arc with a capacitance of 0.02 nF corresponds to the grain boundary region of the material. This analysis is consistent with the established bricklayer model in terms of the capacitance value for bulk and grain boundary regions.[8]

The conductivities of Li_8SnO_6 were determined for both *ex situ* and *in situ* impedance measurements (Fig. 7). The *ex situ* and *in situ* impedance results demonstrate consistency within error limits (Table S3†), and the respective extrapolated overall conductivities at room temperature ($\approx 10^{-9}$ S cm^{-1}) are two orders of magnitude higher than previously reported

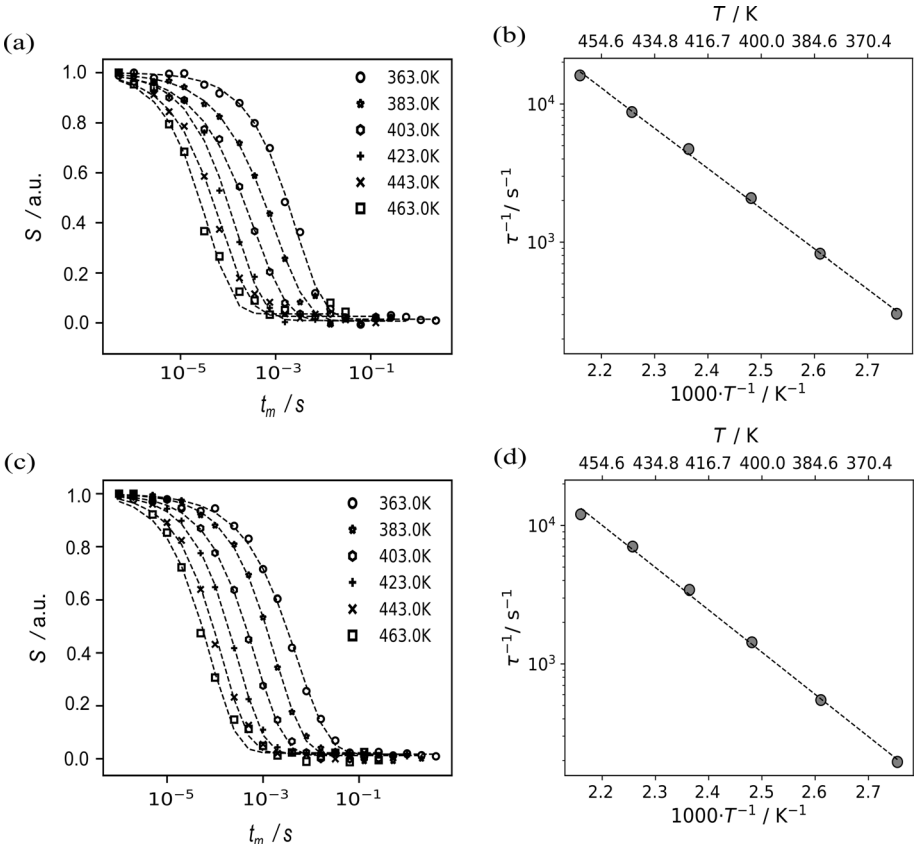

Fig. 5 Results from ^{7}Li spin alignment echo NMR of Li_8SnO_6 at a Larmor frequency of 116.643 MHz. The diagrams on the left show ^{7}Li spin-alignment echo amplitude $S(T,t_m)$ as a function of the mixing time t_m at different temperatures T in the range from 363 to 463 K for the *ex situ* (bottom, c) and the *in situ* setup (top, a). From those measurements, jump rates $1/\tau$ were estimated by fitting a stretched exponential (dashed lines, left column) into the data at individual temperatures. Plots of the resulting jump rate as a function of the inverse temperature are shown on the right (b and d). The dashed fitted lines on the right correspond to an Arrhenius function (see main text).The pre-exponential factor τ_0^{-1} for both *ex situ* and *in situ* is $5.26(4)\cdot10^{10}$ s^{-1} and $3.20(3)\cdot10^{10}$ s^{-1}, respectively.

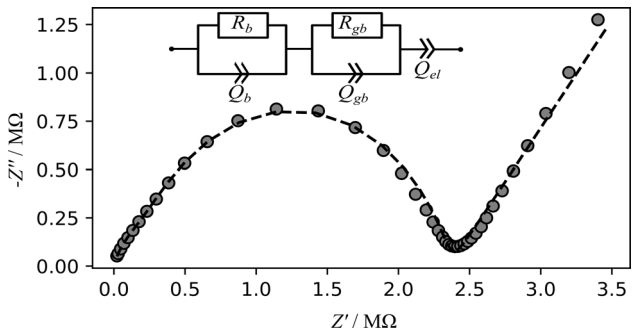

Fig. 6 Exemplary Nyquist (imaginary part of the impedance against real part) plot of impedance measurements for the *in situ* setup conducted on a Li_8SnO_6 pellet (diameter = 8 mm, thickness = 2.1 mm) at a temperature of 393 K. The grey cycles represent the experimental data while dashed line represents the result of fit using the shown model. R_b and R_{gb} are the bulk and grain boundary resistance while Q_b, Q_{gb} and Q_{el} represent the constant phase elements for the bulk, grain boundary and the electrode polarisation, respectively.

conductivity of $3.7\cdot10^{-11}$ S cm^{-1},[31] which can be ascribed to differences in the sample preparation.[19]

An excellent agreement of results from the *ex situ* and *in situ* setup was observed for impedance spectroscopy, ^{7}Li NMR spin-alignment measurements and ^{7}Li NMR line-shape analysis (Tables 2, and S4†), which means that the target of the study to establish a reliable *in situ* EIS–NMR setup was achieved.

What remains to be done is to give meaning to the different observations. Qualitatively, spin-alignment echo NMR and impedance spectroscopy show low jump rates and a rather disappointingly bulk low ion conductivity. An excellent agreement between the activation energies of about 0.60 eV of these two techniques is observed, which indicates that the long-range ion-transport as probed by EIS is limited by the local Li hopping motion probed by NMR.

3.3 Activation energies for Li_8SnO_6 from quantum chemical calculations

Nudged elastic band (NEB) calculations as implemented in quantum espresso (QE) were employed to identify and analyse potential pathways of lithium vacancy migration and to estimate the activation energies of Li_8SnO_6.[31] Lithium cations are distributed over repeating units of one octahedral crystallographic orbit Li_{octa} and one tetrahedral orbit Li_{tetra} in the crystal structure of Li_8SnO_6 (Fig. 8). Macroscopic conduction requires pathways to cover the complete unit cell for example in *c*-direction (Fig. 8) that is crossing the tetrahedral Li-layer like

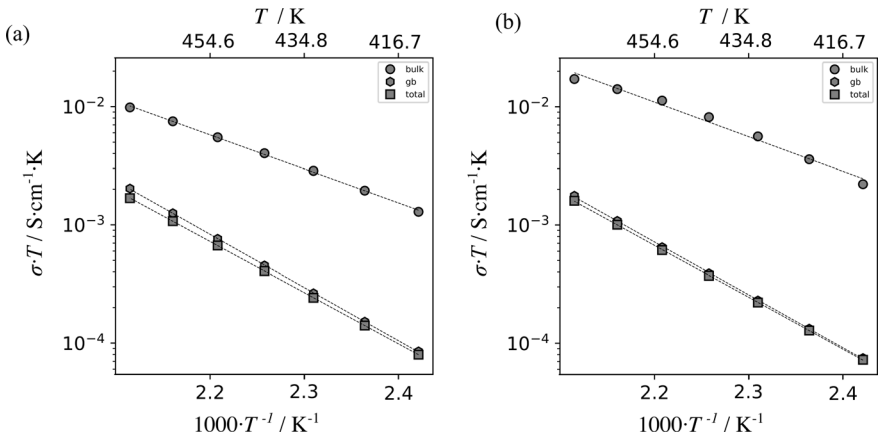

Fig. 7 Plot of the product of electrical conductivity σ and temperature T *versus* inverse temperature for Li_8SnO_6 as measured using a standard, *ex situ* impedance spectroscopy setup (a) and the described *in situ* NMR–EIS setup (b). The results were obtained from impedance spectra in temperature range from 413 K to 473 K. Linear fits are indicated by dashed lines. The data points are indicated by grey circles, hexagons and squares which correspond to bulk, grain boundary and total ionic conductivity values, respectively. The calculated activation energies are shown in Table S3.†

Table 2 Activation energies E_A obtained by ^{7}Li NMR and EIS spectroscopy using the described *ex situ* and *in situ* setups (Fig. 4–6). For the error analysis, a 10% error margin is associated with the line shape analysis based on the Waugh–Fedin theory,[62,63] while the errors for spin-alignment and EIS correspond to the standard errors obtained from the Arrhenius fit

Technique	$E_A^{in\ situ}$/eV	$E_A^{ex\ situ}$/eV
^{7}Li NMR line shape analysis of T_{onset}	0.63(6)	0.62(6)
^{7}Li NMR spin-alignment echo	0.58(1)	0.61(1)
Impedance spectroscopy of bulk conductivity	0.58(3)	0.569(8)

arrangement and passing the octahedral Li sites, or in *a*/*b*-direction that is either within the tetrahedral layer (Fig. S13(b)†) or within the octahedral layer (Fig. S14†).

While the results from the nudged elastic band (NEB) calculation as implemented in quantum espresso (QE) used in this work, are consistent with previously obtained activation energies as implemented in Vienna *ab initio* simulation package (VASP)[32] and classical force field simulations as established in the general utility lattice program (GULP)[33] code (Table 3), we were not able to reconstruct the pathways over a complete unit cell from the information presented in these articles.

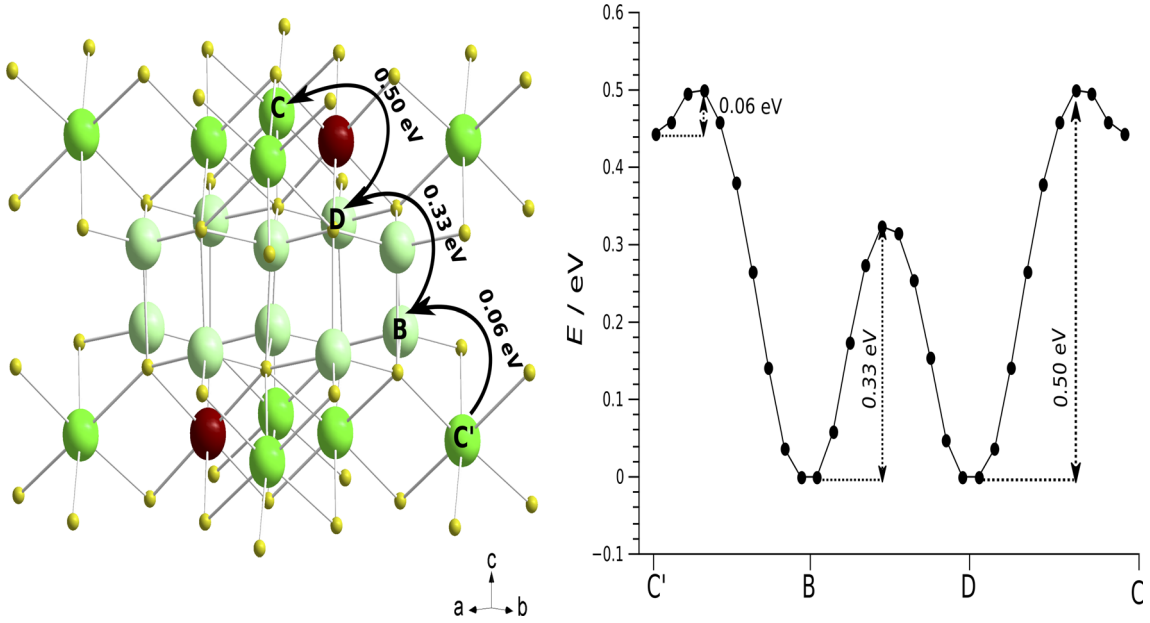

Fig. 8 Potential pathways of vacancy-based Li migration and the associated activation energies determined by Nudged Elastic Band (NEB) calculations. Left: Li-diffusion transport routes from A → B → C → D through a complete unit cell of Li_8SnO_6. The solid arrows represent the most favorable long-range Li ion diffusion pathway in the sense of featuring the lowest maximum activation energy. Right: The graph shows the energy barriers corresponding to the path depicted on the left and the points in the graph correspond to different NEB images along the path.

Table 3 Calculated activation energy E_A barriers for forward and reverse lithium vacancy migration through different crystallographic orbits *via* techniques such as: nudged elastic band (NEB) as implemented in quantum espresso (QE), as implemented in Vienna *ab initio* simulation package (VASP) and classical force field simulations as implemented in the general utility lattice program (GULP)

		E_A/eV						
Techniques	Direction	$Li_{tetra1} \rightarrow Li_{tetra1}$ C → G[b]	$Li_{tetra2} \rightarrow Li_{tetra2}$ B → E[b]	$Li_{tetra1} \rightarrow Li_{tetra2}$ B → C	$Li_{octa} \rightarrow Li_{tetra1}$ A → B	$Li_{tetra2} \rightarrow Li_{octa}$ C → D	$Li_{octa} \rightarrow Li_{octa}$ F → F[b]	Reference
NEB-QE	Forward	0.72	0.72	0.33	0.06	0.5	0.98	This work
	Reverse	0.72	0.72	0.33	0.5	0.06	0.98	
NEB-VASP[a]	Forward	—	—	0.4	—	0.51	0.88	32
	Reverse	—	—	0.43	—	0.04	0.88	
GULP	Forward	0.6	0.6	0.2	0.59	0.59	1.06	33
	Reverse	0.6	0.6	0.2	0.59	0.59	1.06	

[a] The dashes indicate the data in the corresponding literature are missing. [b] The potential pathways of vacancy-based Li vacancy migration and the associated activation energies determined by Nudged Elastic Band calculations are shown in Fig. S13–S15.

From a comparison of three possible pathways covering a complete unit cell (Fig. 8, S13, and S14†), it can be concluded that the preferred lithium vacancy diffusion pathway is along the *c*-direction through $Li_{octa} \rightarrow Li_{tetra1} \rightarrow Li_{tetra2} \rightarrow Li_{octa}$ (A → B → C → D) with a maximum activation energy of 0.50 eV (Fig. 8), while the next lower activation energy of 0.72 eV corresponds to diffusion within the layer-like arrangement of tetrahedrally coordinated Li atoms and the most unlikely motion is motion only within the layer-like arrangement of octahedrally coordinated Li atoms (0.98 eV). This conclusion is only valid if it is assumed that the bottleneck is determined by the activation energies and not by the attempt frequencies. Further, it should be noted that the quantum-chemical calculations are performed at a temperature of 0 K which is far from the experimental conditions and may explain the observed differences. Qualitatively, the experimental activation energy of about 0.60 eV for a macroscopic Li motion is in good agreement with the activation energy of 0.5 eV found by the NEB calculations.

4 Conclusions

In this work, a new setup for *in situ* ^{7}Li NMR–EIS spectroscopy is presented and validated against *ex situ* experiments. It is shown in results on Li_8SnO_6 and $Li_{1.5}Al_{0.5}Ge_{1.5}(PO_4)_3$ that *in situ* NMR–EIS experiments can be conducted to exclude the sample preparation and thermal history as possible explanations for differences between different measurement techniques including NMR line-shape analysis, spin-alignment echo NMR, impedance spectroscopy and in principle also NMR relaxometry. NMR–EIS spectroscopy was applied to the material Li_8SnO_6 and consistent results for the activation energy were obtained by three independent experimental techniques. With the help of nudged elastic band calculations for the first time, a consistent interpretation of obtained activation energies of Li_8SnO_6 is provided. It is anticipated that NMR–EIS spectroscopy will help to resolve discrepancies based on sample related changes such as thermally induced irreversible changes or ageing effects in solid ion conductors. Furthermore, it can be applied to study metastable intermediaries in solid ion conductors.

Author contributions

Conceptualization: JSADG; investigation: SCA and NM; writing original draft: SCA and NM; writing – review and editing: JSADG; visualization: SCA and NM; funding acquisition: JSADG, SCA; supervision: JSADG.

Conflicts of interest

There are no conflicts to declare.

Acknowledgements

We thank Andreas Neuberger and Xu Ke for their help in getting started with the electrical parts and 3D printing, respectively. The brass parts were produced by the mechanical workshop of the University of Siegen. Financial support by the House of Young Talents, University of Siegen is acknowledged.

References

1 J. B. Goodenough, *J. Solid State Electrochem.*, 2012, **16**, 2019–2029.
2 Y. Kato, S. Hori, T. Saito, K. Suzuki, M. Hirayama, A. Mitsui, M. Yonemura, H. Iba and R. Kanno, *Nat. Energy*, 2016, **1**, 1–7.
3 J. Janek and W. G. Zeier, *Nat. Energy*, 2016, **1**, 16141.
4 Z. Zhang, Y. Shao, B. Lotsch, Y.-S. Hu, H. Li, J. Janek, L. F. Nazar, C.-W. Nan, J. Maier, M. Armand and L. Chen, *Energy Environ. Sci.*, 2018, **11**, 1945–1976.
5 P. Heitjans and S. Indris, *J. Phys.: Condens. Matter*, 2003, **15**, R1257.
6 Y. Gao, A. M. Nolan, P. Du, Y. Wu, C. Yang, Q. Chen, Y. Mo and S.-H. Bo, *Chem. Rev.*, 2020, **120**, 5954–6008.
7 Z.-H. Fu, X. Chen and Q. Zhang, *Wiley Interdiscip. Rev.: Comput. Mol. Sci.*, 2023, **13**, e1621.
8 J. T. S. Irvine, D. C. Sinclair and A. R. West, *Adv. Mater.*, 1990, **2**, 132–138.
9 E. O. Stejskal and J. E. Tanner, *J. Chem. Phys.*, 2004, **42**, 288–292.

10 C. S. Johnson, *Prog. Nucl. Magn. Reson. Spectrosc.*, 1999, **34**, 203–256.
11 R. Böhmer, K. R. Jeffrey and M. Vogel, *Prog. Nucl. Magn. Reson. Spectrosc.*, 2007, **50**, 87–174.
12 Y.-X. Xiang, G. Zheng, G. Zhong, D. Wang, R. Fu and Y. Yang, *Solid State Ionics*, 2018, **318**, 19–26.
13 M. Wilkening, R. Amade, W. Iwaniak and P. Heitjans, *Phys. Chem. Chem. Phys.*, 2007, **9**, 1239–1246.
14 N. Bloembergen, E. M. Purcell and R. V. Pound, *Phys. Rev.*, 1948, **73**, 679–712.
15 M. Wilkening, C. Mühle, M. Jansen and P. Heitjans, *J. Phys. Chem. B*, 2007, **111**, 8691–8694.
16 M. Wilkening, A. Kuhn and P. Heitjans, *Phys. Rev. B: Condens. Matter Mater. Phys.*, 2008, **78**, 054303.
17 M. Tatsumisago, C. A. Angell and S. W. Martin, *J. Chem. Phys.*, 1992, **97**, 6968–6974.
18 K. L. Ngai and C. León, *J. Non-Cryst. Solids*, 2003, **315**, 124–133.
19 S. Ohno, T. Bernges, J. Buchheim, M. Duchardt, A.-K. Hatz, M. A. Kraft, H. Kwak, A. L. Santhosha, Z. Liu, N. Minafra, F. Tsuji, A. Sakuda, R. Schlem, S. Xiong, Z. Zhang, P. Adelhelm, H. Chen, A. Hayashi, Y. S. Jung, B. V. Lotsch, B. Roling, N. M. Vargas-Barbosa and W. G. Zeier, *ACS Energy Lett.*, 2020, **5**, 910–915.
20 P. G. Bruce and A. R. West, *J. Solid State Chem.*, 1982, **44**, 354–365.
21 H. Y.-P. Hong, *Mater. Res. Bull.*, 1978, **13**, 117–124.
22 J. G. Kamphorst and E. E. Hellstrom, *Solid State Ionics*, 1980, **1**, 187–197.
23 R. Murugan, V. Thangadurai and W. Weppner, *Angew. Chem., Int. Ed.*, 2007, **46**, 7778–7781.
24 A. Kuhn, V. Epp, G. Schmidt, S. Narayanan, V. Thangadurai and M. Wilkening, *J. Phys.: Condens. Matter*, 2011, **24**, 035901.
25 A. Kuhn, S. Narayanan, L. Spencer, G. Goward, V. Thangadurai and M. Wilkening, *Phys. Rev. B: Condens. Matter Mater. Phys.*, 2011, **83**, 094302.
26 K. Meier, T. Laino and A. Curioni, *J. Phys. Chem. C*, 2014, **118**, 6668–6679.
27 R. Jalem, Y. Yamamoto, H. Shiiba, M. Nakayama, H. Munakata, T. Kasuga and K. Kanamura, *Chem. Mater.*, 2013, **25**, 425–430.
28 M. Xu, M. S. Park, J. M. Lee, T. Y. Kim, Y. S. Park and E. Ma, *Phys. Rev. B: Condens. Matter Mater. Phys.*, 2012, **85**, 052301.
29 M. Troemel and J. Hauck, *Z. Anorg. Allg. Chem.*, 1969, **368**, 248–253.
30 R. Hoppe and R. M. Braun, *Z. Anorg. Allg. Chem.*, 1977, **433**, 181–188.
31 J. Senegas, A. M. Villepastour and C. Delmas, *J. Solid State Chem.*, 1980, **31**, 103–112.
32 N. Luo, Z. Hou, C. Zheng, Y. Zhang, A. Stein, S. Huang and D. G. Truhlar, *Chem. Mater.*, 2021, **33**, 834–844.
33 N. Kuganathan, A. L. Solovjov, R. V. Vovk and A. Chroneos, *Heliyon*, 2021, **7**, e07460.
34 O. Pecher, J. Carretero-González, K. J. Griffith and C. P. Grey, *Chem. Mater.*, 2017, **29**, 213–242.
35 F. Chevallier, M. Letellier, M. Morcrette, J.-M. Tarascon, E. Frackowiak, J.-N. Rouzaud and F. Béguin, *Electrochem. Solid-State Lett.*, 2003, **6**, A225.
36 K. Märker, C. Xu and C. P. Grey, *J. Am. Chem. Soc.*, 2020, **142**, 17447–17456.
37 F. Chevallier, F. Poli, B. Montigny and M. Letellier, *Carbon*, 2013, **61**, 140–153.
38 M. Letellier, F. Chevallier, F. Béguin, E. Frackowiak and J.-N. Rouzaud, *J. Phys. Chem. Solids*, 2004, **65**, 245–251.
39 M. Letellier, F. Chevallier and M. Morcrette, *Carbon*, 2007, **45**, 1025–1034.
40 B. Key, R. Bhattacharyya, M. Morcrette, V. Seznéc, J.-M. Tarascon and C. P. Grey, *J. Am. Chem. Soc.*, 2009, **131**, 9239–9249.
41 J. Arai, K. Gotoh, R. Sayama and K. Takeda, *J. Electrochem. Soc.*, 2017, **164**, A6334–A6340.
42 R. Bhattacharyya, B. Key, H. Chen, A. S. Best, A. F. Hollenkamp and C. P. Grey, *Nat. Mater.*, 2010, **9**, 504–510.
43 J. Nasir, N. Steinbrück, K. Xu, B. Engelen and J. Schmedt auf der Günne, *J. Appl. Crystallogr.*, 2022, **55**, 1097–1103.
44 A. A. Coelho, J. Evans, I. Evans, A. Kern and S. Parsons, *Powder Diffr.*, 2011, **26**, S22–S25.
45 R. K. Harris, E. D. Becker, S. M. Cabral De Menezes, R. Goodfellow and P. Granger, *Concepts Magn. Reson.*, 2002, **14**, 326–346.
46 R. K. Harris, E. D. Becker, S. M. Cabral de Menezes, P. Granger, R. E. Hoffman and K. W. Zilm, *Pure Appl. Chem.*, 2008, **80**, 59–84.
47 J. Jeener and P. Broekaert, *Phys. Rev.*, 1967, **157**, 232–240.
48 F. Qi, G. Diezemann, H. Böhm, J. Lambert and R. Böhmer, *J. Magn. Reson.*, 2004, **169**, 225–239.
49 S. Faske, B. Koch, S. Murawski, R. Küchler, R. Böhmer, J. Melchior and M. Vogel, *Phys. Rev. B: Condens. Matter Mater. Phys.*, 2011, **84**, 024202.
50 D. Jardón-Álvarez and J. Schmedt auf der Günne, *Solid State Nucl. Magn. Reson.*, 2018, **94**, 26–30.
51 P. Virtanen, R. Gommers, T. E. Oliphant, M. Haberland, T. Reddy, D. Cournapeau, E. Burovski, P. Peterson, W. Weckesser, J. Bright, S. J. van der Walt, M. Brett, J. Wilson, K. J. Millman, N. Mayorov, A. R. J. Nelson, E. Jones, R. Kern, E. Larson, C. J. Carey, İ. Polat, Y. Feng, E. W. Moore, J. VanderPlas, D. Laxalde, J. Perktold, R. Cimrman, I. Henriksen, E. A. Quintero, C. R. Harris, A. M. Archibald, A. H. Ribeiro, F. Pedregosa and P. van Mulbregt, *Nat. Methods*, 2020, **17**, 261–272.
52 P. Giannozzi, O. Baseggio, P. Bonfà, D. Brunato, R. Car, I. Carnimeo, C. Cavazzoni, S. de Gironcoli, P. Delugas, F. Ferrari Ruffino, A. Ferretti, N. Marzari, I. Timrov, A. Urru and S. Baroni, *J. Chem. Phys.*, 2020, **152**, 154105.
53 T. Björkman, *Comput. Phys. Commun.*, 2011, **182**, 1183–1186.
54 K. F. Garrity, J. W. Bennett, K. M. Rabe and D. Vanderbilt, *Comput. Mater. Sci.*, 2014, **81**, 446–452.
55 J. W. Bennett, B. G. Hudson, I. K. Metz, D. Liang, S. Spurgeon, Q. Cui and S. E. Mason, *Comput. Mater. Sci.*, 2019, **170**, 109137.

56 H. J. Monkhorst and J. D. Pack, *Phys. Rev. B: Solid State*, 1976, **13**, 5188–5192.
57 G. Henkelman, B. P. Uberuaga and H. Jónsson, *J. Chem. Phys.*, 2000, **113**, 9901–9904.
58 A. J. Ilott, S. Chandrashekar, A. Klöckner, H. J. Chang, N. M. Trease, C. P. Grey, L. Greengard and A. Jerschow, *J. Magn. Reson.*, 2014, **245**, 143–149.
59 B. J. Walder, M. S. Conradi, J. J. Borchardt, L. C. Merrill, E. G. Sorte, E. J. Deichmann, T. M. Anderson, T. M. Alam and K. L. Harrison, *Sci. Adv.*, 2021, **7**, eabg8298.
60 J. Schaefer, and R. A. McKay, Multi-Tuned Single Coil Transmission Line Probe for Nuclear Magnetic Resonance Spectrometer, *US Pat.*, US5861748A, 1999.
61 N. Meddings, M. Heinrich, F. Overney, J.-S. Lee, V. Ruiz, E. Napolitano, S. Seitz, G. Hinds, R. Raccichini, M. Gaberšček and J. Park, *J. Power Sources*, 2020, **480**, 228742.
62 J. S. Waugh and E. I. Fedin, *Fiz. Tverd. Tela*, 1962, **4**, 2233–2237.
63 J. S. Waugh and E. I. Fedin, *Phys. Solid State*, 1963, **4**, 1633–1636.
64 F. Qi, T. Jörg and R. Böhmer, *Solid State Nucl. Magn. Reson.*, 2002, **22**, 484–500.
65 S. Faske, H. Eckert and M. Vogel, *Phys. Rev. B: Condens. Matter Mater. Phys.*, 2008, **77**, 104301.
66 G. J. Brug, A. L. G. van den Eeden, M. Sluyters-Rehbach and J. H. Sluyters, *J. Electroanal. Chem. Interfacial Electrochem.*, 1984, **176**, 275–295.